

# Computing excited states of molecules using normalizing flows

Yahya Saleh,<sup>1,2,\*</sup> Álvaro Fernández Corral,<sup>2,3</sup> Emil Vogt,<sup>2</sup>  
Armin Iske,<sup>1</sup> Jochen Küpper,<sup>2,3,4</sup> and Andrey Yachmenev<sup>2,4,†</sup>

<sup>1</sup>*Department of Mathematics, Universität Hamburg, Bundesstr. 55, 20146, Hamburg, Germany*

<sup>2</sup>*Center for Free-Electron Laser Science CFEL, Deutsches*

*Elektronen-Synchrotron DESY, Notkestr. 85, 22607 Hamburg, Germany*

<sup>3</sup>*Department of Physics, Universität Hamburg, Luruper Chaussee 149, 22761 Hamburg, Germany*

<sup>4</sup>*Center for Ultrafast Imaging, Universität Hamburg, Luruper Chaussee 149, 22761 Hamburg, Germany*

(Dated: 2024-11-12)

Calculations of highly excited and delocalized molecular vibrational states is a computationally challenging task, which strongly depends on the choice of coordinates for describing vibrational motions. We introduce a new method that utilizes normalizing flows—parametrized invertible functions—to optimize vibrational coordinates to satisfy the variational principle. This approach produces coordinates specifically tailored to the vibrational problem at hand, significantly increasing the accuracy and enhancing basis set convergence of calculated energy spectrum. The efficiency of the method is demonstrated in calculations of the 100 lowest excited vibrational states of H<sub>2</sub>S, H<sub>2</sub>CO, and HCN/CNH. The method effectively captures the essential vibrational behavior of molecules by enhancing the separability of the Hamiltonian. We further demonstrate that the optimized coordinates are transferable across different levels of basis set truncation, enabling a cost-efficient protocol for computing vibrational spectra of high-dimensional systems.

Accurate calculations of highly excited vibrational states of polyatomic molecules are essential for unravelling increasingly rich experimental spectroscopic information and understanding the dynamics of intermolecular motions. The highly excited molecular vibrations are especially important in fields such as chemical reactivity [1–3] and collisions [4, 5], relaxation processes [6] and stimulated emission [7], as well as spectroscopic probing of high-temperature environments found on exoplanets [8, 9] and industrial applications [10, 11].

A range of variational and perturbative methods were developed for predicting vibrational spectra of molecules [12–18]. These methods solve the eigenvalue problem for a vibrational Hamiltonian, which is constructed using appropriately chosen vibrational coordinates. The choice of coordinates is a crucial task that directly affects the accuracy of energy calculations. When using a direct product basis of univariate functions, a key challenge is selecting coordinates that provide a large degree of separability of vibrational motions, thereby reducing the computational effort required to solve the vibrational eigenvalue problem [19]. This is particularly important for calculations of delocalized vibrational states of floppy molecules [20, 21], such as van der Waals complexes [22], molecules near dissociation [23], and high-energy excitations in general [24], where couplings between different vibrational modes are much more prominent.

Rectilinear normal coordinates provide a natural starting point for seeking separability in vibrational problems. However, they become less effective for highly excited states and are generally not suited for floppy molecules, e. g., weakly bound complexes, which naturally sample configurations far from their reference equilibrium geom-

etry. Alternative curvilinear coordinate systems, such as Radau [25], Jacobi [26, 27], valence [28], and polyspherical [29–31] coordinates, were successfully applied in the vibrational calculations of various floppy polyatomic molecules [13, 32]. Choosing the optimal coordinates requires a combination of intuition, consideration of the symmetries of the system, and prior knowledge of the potential energy landscape. This task is particularly challenging for floppy molecules and generally large systems. Several general strategies were recently developed to guide the selection and design of vibrational coordinates, drawing from the available pool of known curvilinear and rectilinear coordinates [33–35].

Due to the diversity of nuclear motions and their dependence on molecular size and bonding topology, no single coordinate system is universally optimal for describing the vibrations of different molecules. One promising approach to improve the effectiveness of a coordinate system involves developing general coordinates, parametrized by variables that can be optimized to minimize vibrational couplings or energy levels. Such general coordinates, expressed as linear combinations of normal [36, 37] or curvilinear [38–44] coordinates, were shown to significantly enhance the accuracy of variational calculations. Despite these developments, the broader application of coordinate optimization in variational calculations remains largely unexplored, with previous efforts limited to linear parametrizations specific to particular systems.

In this work, we introduce a new general nonlinear parametrization for vibrational coordinates that is based on normalizing flows [45], implemented using a neural network. The parameters of the neural network are optimized using the variational principle. Applied to the calculation of the 100 lowest vibrational states in H<sub>2</sub>S,

H<sub>2</sub>CO, and HCN/CNH molecules, the present approach achieves several orders of magnitude improvements in the accuracy of vibrational energies as compared to the commonly used curvilinear coordinates. The optimized vibrational coordinates effectively capture the underlying physics of the problem, reduce couplings between different vibrational modes, and remain consistent across various levels of basis set truncation. Building on this property, we proposed a cost-efficient approach in which the coordinates are first optimized using a small basis set and then applied to calculations with a larger basis set, keeping the parameters fixed.

We begin by choosing a truncated set of orthonormal basis functions  $\{\phi_n(\mathbf{r})\}_{n=0}^N$  of  $L^2$  along with an invertible map  $g_\theta$  parametrized by a set of parameters  $\theta$ .  $g_\theta$  maps an initial set of vibrational coordinates  $\mathbf{r}$  to a new set of coordinates  $\mathbf{q}$  of the same dimension, i. e.,  $\mathbf{q} = g_\theta(\mathbf{r})$ . To improve the approximation properties of the basis functions  $\phi_n$ , we evaluate them in  $\mathbf{q}$  to obtain a new set of augmented basis functions  $\{\gamma_n(\mathbf{q}; \theta)\}_{n=0}^N$  defined as

$$\gamma_n(\mathbf{q}; \theta) := \phi_n(\mathbf{q}) \sqrt{|1/\det \nabla_{\mathbf{q}} g_\theta^{-1}(\mathbf{q})|}, \quad (1)$$

where multiplying by the inverse of the square root of the determinant of the Jacobian ensures that the basis functions remain orthonormal with respect to the  $L^2$ -inner product, independent of the values of  $\theta$ . Inducing augmented basis functions by a nonlinear change of variable is analogous to inducing an augmented probability distribution  $p$  from a base distribution  $p_0$  using a change of variables  $g_\theta$ , commonly referred to as a normalizing flow in the machine learning literature [45, 46]. Therefore, we refer to  $g_\theta$  as a normalizing flow in the context of this work.

The matrix elements of the vibrational kinetic and potential energy operators in the augmented basis (1) can be expressed by introducing a change of variables  $\mathbf{q} = g_\theta(\mathbf{r})$  in the integrals. For the potential, this results in the following expression

$$\mathbf{V}_{n'n} = \langle \gamma_{n'} | V | \gamma_n \rangle = \int \phi_{n'}^*(\mathbf{q}) V(g_\theta^{-1}(\mathbf{q})) \phi_n(\mathbf{q}) d\mathbf{q}. \quad (2)$$

This illustrates that the normalizing flow  $g_\theta$  effectively modifies the coordinates in which the operators are expressed for a fixed set of basis functions  $\{\phi\}_n$ . The corresponding expression for the kinetic energy operator is provided in the supplementary information.

The map  $g_\theta$  can, in principle, be any differentiable invertible function. However, to maintain the completeness of the augmented basis set  $\{\gamma_n(\mathbf{q}; \theta)\}_{n=0}^\infty$ , the normalizing flow must be bi-Lipschitz [47]. This means that there exist constants  $k, K > 0$  such that  $k \leq |\det \nabla_{\mathbf{r}} g_\theta(\mathbf{r})| \leq K$  for all  $\mathbf{r}$ . We construct  $g_\theta$  as an invertible residual neural network (iResNet) [48], which by construction satisfies the bi-Lipschitz requirement. We refer to the supplementary information for a more detailed explanation of the

equivalence between optimizing basis sets and vibrational coordinates.

We approximate the vibrational wavefunctions  $\Psi_m$  ( $m = 1..M$ ) as linear combination of augmented basis functions (1), i. e.,

$$\Psi_m(\mathbf{q}) \approx \sum_{n \leq N} c_{nm} \gamma_n(\mathbf{q}; \theta). \quad (3)$$

The linear-expansion coefficients  $c_{nm}$  and the normalizing flow parameters  $\theta$  are determined using the variational principle, by minimizing the energies of the ground and excited vibrational states. For the coefficients, this is equivalent to solving the eigenvalue problem  $\mathbf{E} = \mathbf{C}^{-1} \mathbf{H} \mathbf{C}$ , where  $\mathbf{C} = \{c_{nm}\}_{n,m}^{N,M}$ ,  $\mathbf{E} = \{E_m\}_m^M$  are the vibrational energies, and  $\mathbf{H} = \mathbf{T} + \mathbf{V}$  is the sum of matrix representations of the kinetic and potential energy operators in the augmented basis set (1).

Because vibrational energies are nonlinear functions of parameters  $\theta$ , these parameters are optimized using gradient descent methods. The optimization is guided by a loss function derived from the variational principle and may involve minimizing quantities such as the sum of vibrational energies, the trace of the Hamiltonian matrix, or the matrix exponential. A loss function expressed as the sum of all energies spanned by the chosen basis set is equivalent to the trace of the Hamiltonian matrix,

$$\mathcal{L}_\theta = \sum_{n \leq N} E_n = \text{Tr}(\mathbf{H}) \rightarrow \min_{\theta}. \quad (4)$$

This loss function has a relatively low computational cost, as it decouples the nonlinear parameters  $\theta$  from the eigenvector coefficients  $c_{nm}$ , requiring only the evaluation of diagonal elements of the Hamiltonian matrix when the initial basis is orthonormal. In contrast, when the loss function is based on the sum of a subset of the lowest energies, the parameters depend on the eigenvector coefficients  $c_{nm}$ , and a repeated solution of the eigenvalue problem during optimization is required. Despite the added complexity, the high accuracy achieved even with small basis sets can outweigh the computational costs of the repeated matrix diagonalization.

The evaluation of the matrix elements in (2) and the analogous expression for the kinetic energy operator is one of the most computationally demanding parts. In this work, we employed Gaussian quadratures to compute the necessary integrals, altering the quadrature degree at different optimization steps to prevent overfitting. We found that alternating between smaller quadratures during optimization was computationally more efficient while still converging to the same values of the parameters  $\theta$  as those obtained using a larger quadrature. After convergence, the final energies and wavefunctions were computed by solving the eigenvalue problem with a large quadrature for accurate integral evaluations. For higher-dimensional systems, more efficient techniques such as sparse-grid

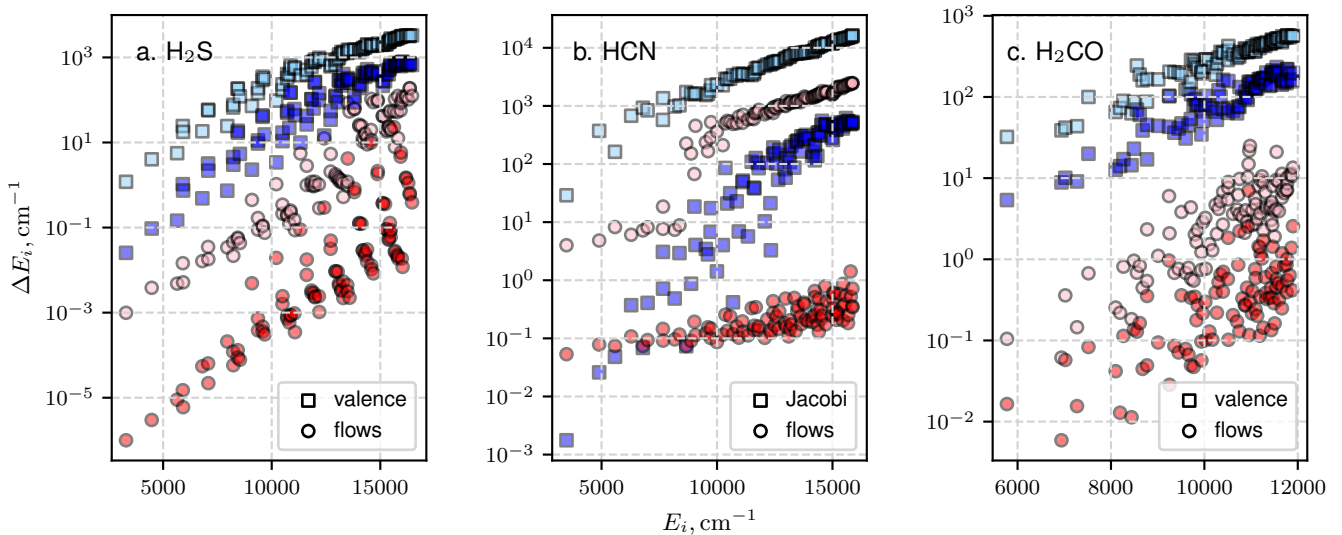


FIG. 1. Convergence of the 100 lowest vibrational energy levels ( $E_i$ ,  $i = 1..100$ ) for H<sub>2</sub>S (a), HCN/CNH (b), and H<sub>2</sub>CO (c), using standard valence or Jacobi vibrational coordinates (blue squares) compared to optimized normalizing-flow coordinates (red circles). The energy discrepancies ( $\Delta E_i$ ) between the calculated and benchmark energies are shown for two basis sets, truncated at  $P_{\max} = 12$  (140 basis functions) and 20 (506) for H<sub>2</sub>S, at  $P_{\max} = 12$  (140) and 32 (1785) for HCN, and at  $P_{\max} = 9$  (1161) and 12 (3900) for H<sub>2</sub>CO. Lighter and darker colors represent the smaller and larger basis sets, respectively.

methods [49] or collocation [50] can be used. Alternatively, Monte-Carlo methods [51, 52] may be employed when high accuracy is not required.

The accuracy and performance of our approach were validated in calculations of vibrational states for hydrogen sulfide H<sub>2</sub>S, formaldehyde H<sub>2</sub>CO, and hydrogen cyanide/hydrogen isocyanide HCN/CNH isomers. For H<sub>2</sub>S and H<sub>2</sub>CO, we used valence coordinates as the reference coordinates and employed a direct product of Hermite functions as the basis set. The direct product basis was constructed by considering only combinations of one-dimensional vibrational quantum numbers ( $n_1, n_2, n_3$ ) that satisfy the polyad condition  $2n_1 + 2n_2 + n_3 \leq P_{\max}$ , where  $n_1, n_2$ , and  $n_3$  correspond to the vibrational quanta for  $r_{\text{SH}_1}$ ,  $r_{\text{SH}_2}$ , and  $\alpha_{\angle \text{H}_1\text{SH}_2}$  valence coordinates, respectively. For H<sub>2</sub>CO, we applied the basis truncation condition  $2n_1 + 2n_2 + 2n_3 + n_4 + n_5 + n_6 \leq P_{\max}$ , where  $n_1, \dots, n_6$  correspond to the vibrational quanta for valence coordinates  $r_{\text{CO}}, r_{\text{CH}_1}, r_{\text{CH}_2}, \alpha_{\angle \text{OCH}_1}, \alpha_{\angle \text{OCH}_2}$ , and  $\tau$ , the dihedral angle between the OCH<sub>1</sub> and OCH<sub>2</sub> planes. For HCN/CNH, we used Jacobi reference coordinates  $r_{\text{CN}}, R, \alpha_{\angle \text{R-CN}}$ , where  $R$  is the distance between the hydrogen atom and the center of mass of the C–N bond, and  $\alpha_{\angle \text{R-CN}}$  is the angle between these coordinate vectors. We used Hermite functions for the two radial coordinates and Legendre functions for the angular coordinate. The Legendre functions were multiplied by  $\sin^{1/2}(\alpha_{\angle \text{R-CN}})$  to ensure the correct behaviour of the wavefunction at the linear geometry of the molecule, where the Hamiltonian becomes singular [53, 54]. For all molecules, we employed spectroscopically refined potential energy surfaces (PES) [55–57]

and numerically constructed exact kinetic energy operator using the method described in [13, 24].

To model the normalizing flow  $g_\theta$ , we used an iResNet consisting of 10 blocks. Each block was represented by a dense neural network comprising two hidden layers with unit sizes [8, 8] and an output layer of  $n$  units, where  $n$  corresponds to the number of coordinates. A complete description and diagram of the normalizing flow architecture is available in the supplementary information. The flow parameters were optimized variationally by minimizing the sum of the 100 lowest vibrational energies, using the basis sets truncated at  $P_{\max} = 36, 8$ , and 44 for H<sub>2</sub>S, H<sub>2</sub>CO, and HCN/CNH, respectively. For H<sub>2</sub>CO, to balance computational efficiency and accuracy, the final results were computed using a basis truncated at  $P_{\max} = 12$  utilizing flow parameters optimized for the  $P_{\max} = 8$  truncation.

On average, over the 100 lowest energies, the calculations converged with an accuracy of 0.04 cm<sup>-1</sup> for H<sub>2</sub>S, 0.53 cm<sup>-1</sup> for H<sub>2</sub>CO, and 0.03 cm<sup>-1</sup> for HCN/CNH compared to the reference values reported in the literature [55–57]. We thus considered our results to be converged and used them as benchmark data throughout the rest of the manuscript. A table summarizing the deviations of vibrational energies from the reference values is provided in the supplementary information.

The absolute error for the 100 lowest vibrational states of H<sub>2</sub>S, H<sub>2</sub>CO, and HCN/CNH, as a function of the basis set truncation parameter  $P_{\max}$ , is shown in FIG. 1. For each molecule, the results of two variational calculations are presented, one using reference valence or Jacobi coordinates

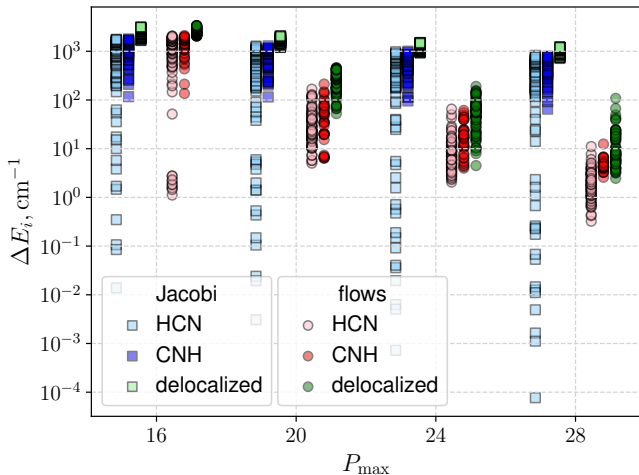


FIG. 2. Convergence of the lowest 200 vibrational energy levels ( $E_i$ ,  $i = 1..200$ ) for HCN/CNH, calculated with Jacobi coordinates (squares) or with optimized normalizing-flow coordinates (circles). The energy discrepancies ( $\Delta E_i$ ) relative to our converged benchmark reference are shown for several basis sets, truncated at  $P_{\max} = 12$  (140 basis functions), 16 (204), 20 (285), 24 (385), and 28 (506). Vibrational states assigned to the HCN isomer, the CNH isomer, and states with an energy above the isomerization barrier (delocalized) are differentiated by color. All states are slightly offset along the  $P_{\max}$  axis for visual clarity.

ordinates and another using the optimized normalizing-flow coordinates. Coordinate optimization resulted in up to four orders of magnitude improvement in the accuracy of vibrational energy calculations compared to using the standard reference coordinates. Extrapolating to larger basis sets, we estimate that matching the same accuracy using the reference coordinates would require approximately an order of magnitude increase in the number of basis functions.

We note that the convergence of results can also be improved by increasing the complexity of the normalizing-flow function. A detailed study of this effect is provided in the supplementary information.

Direct product basis sets can be improved using basis set contraction, which involves partitioning the total Hamiltonian into subsystems, solving reduced-dimensional variational problems for each, and then using these solutions for the full-dimensional problem [58, 59]. For molecules like  $\text{H}_2\text{S}$  and  $\text{H}_2\text{CO}$ , basis set contraction works well due to near-separability of valence vibrational coordinates in the PES. However, this approach becomes more challenging for floppy molecules like HCN/CNH, where two of the Jacobi vibrational coordinates are strongly coupled.

This challenge is illustrated in FIG. 2 for the first 200 vibrational energies of HCN/CNH. The figure presents results of basis set contraction using Jacobi coordinates alongside those obtained with a direct product basis set of primitive functions (i. e., Hermite and Legendre) using

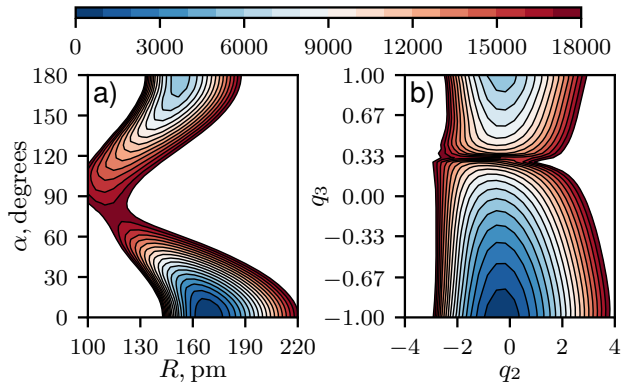


FIG. 3. Two-dimensional cuts of the HCN/CNH potential energy surface: (a) along the Jacobi coordinates  $R$  and  $\alpha_{\angle\text{R-CN}}$  and (b) along the optimized normalizing-flow coordinates. The optimization was performed for a basis set truncated at  $P_{\max} = 16$  (204 basis functions) with the loss function defined as the sum of the 100 lowest vibrational state energies.

optimized normalizing-flow coordinates. The contracted basis was constructed by partitioning the Hamiltonian into one-dimensional subsystems for each of the Jacobi coordinates, with the HCN isomer equilibrium geometry as the reference configuration. As shown in FIG. 2, the contracted basis significantly improves convergence compared to the product basis set results in FIG. 1.b, but not for all vibrational states. High accuracy is only achieved for states localized around the HCN minimum of the PES, while delocalized states and states localized around the CNH minimum show little improvement. In contrast, the optimized normalizing-flow coordinates provide a balanced description of all localized and delocalized states, with a much smaller spread in errors across different states.

To gain insight into the interpretation of the optimized normalizing-flow coordinates, we plotted in FIG. 3 the two-dimensional cut of the PES of HCN/CNH along the strongly coupled Jacobi coordinates,  $R$  and  $\alpha_{\angle\text{R-CN}}$ , i. e.,  $V(r_0, R, \alpha_{\angle\text{R-CN}})$ , alongside the corresponding cut in the optimized normalizing-flow coordinates,  $V(g_\theta^{-1}(q_1, q_2, q_3))$ . In these plots,  $r_{\text{CN}}$  coordinate is fixed at its equilibrium value  $r_0$  and  $q_1 = 0$ . The potential is clearly highly anisotropic when expressed in Jacobi coordinates (panel a), which leads to a strong coupling between the two vibrations. In contrast, when expressed in the optimized coordinates (panel b), the HCN $\leftrightarrow$ CNH minimum energy isomerization pathway is practically a straight line along the coordinate  $q_3$  at  $q_2 \approx 0$ . This reduction in anisotropy explains why coordinate optimization improves the convergence in the product basis. The optimization achieves an effective coordinate decoupling of the PES, which allows for a better approximation of the eigenfunctions of the Hamiltonian by the chosen direct product basis. In addition, it is evident from the spac-

ing between the contour lines along the flows coordinate  $q_2$ , that the potential becomes more harmonic in this dimension in comparison to  $R$  in the Jacobi coordinates. The same behavior was observed for  $q_1$  and  $r_{\text{CN}}$ . This is expected, as Hermite functions—the solutions of the quantum harmonic oscillator—were used as the basis for stretching coordinates.

We found that the converged iResNet parameters remained nearly identical when optimized using different basis set truncations, suggesting that there exist unique optimal vibrational coordinates for a given type of basis. Leveraging this finding, we developed a cost-efficient approach where the flow coordinates are first optimized using a small basis set and then applied with fixed parameters in calculations with larger basis sets. This significantly reduces the computational costs and makes it feasible to apply our approach to high-dimensional systems while maintaining accuracy comparable to full optimization. Results provided in the supplementary information demonstrate the effectiveness of this method. Moreover, the principle of transferability of optimal coordinates could potentially be extended to isotopologues or molecular systems sharing similar structural motifs, contributing to our understanding of intrinsic vibrational coordinates.

In summary, we introduced a general nonlinear parametrization for vibrational coordinates of molecules using normalizing flows. By optimizing the flow parameters through the variational principle, we significantly accelerated basis set convergence, leading to more accurate vibrational energies. The improvement is especially pronounced for highly excited and delocalized vibrational states. Additionally, the learned coordinates enhanced the separability of the PES, potentially allowing for a more intuitive interpretation of the key motifs in strongly-coupled vibrational dynamics. The transferability of these optimized coordinates across different basis set sizes also provides a computationally efficient protocol for larger molecular system calculations. It is worth noting that after the release of the first arXiv version of this work [60], another group integrated the concept of normalizing flows for basis-set augmentation with Monte-Carlo methods and successfully applied it to high-dimensional systems [61].

We also explored the applicability of the normalizing-flow method for excited electronic states, testing it on single-electron systems such as the hydrogen atom, hydrogen molecular ion, and carbon atom in the single-active electron approximation. Results presented in the supplementary information show a significant improvement in basis set convergence. This suggests promising potential of normalizing-flow method for electronic structure problems, especially since neural-network-based methods for excited state computations remain challenging [52, 62].

## ACKNOWLEDGMENTS

We thank Jannik Eggers, Sebastian Nicolas Mendoza, and Vishnu Sanjay for useful comments and discussions in early stages of this work. This work was supported by Deutsches Elektronen-Synchrotron DESY, a member of the Helmholtz Association (HGF), including the Maxwell computational resource operated at DESY, by the Data Science in Hamburg HELMHOLTZ Graduate School for the Structure of Matter (DASHH, HIDSS-0002), and by the Deutsche Forschungsgemeinschaft (DFG) through the cluster of excellence “Advanced Imaging of Matter” (AIM, EXC 2056, ID 390715994). This work was supported by Helmholtz AI computing resources (HAICORE) of the Helmholtz Association’s Initiative and Networking Fund through Helmholtz AI.

---

\* Email: yahya.saleh@cfel.de

† Email: andrey.yachmenev@cfel.de;

URL: <https://www.controlled-molecule-imaging.org>

- [1] Z. Li, Y.-l. Fu, Z. Luo, S. Yang, Y. Wu, H. Wu, G. Wu, W. Zhang, B. Fu, K. Yuan, D. Zhang, and X. Yang, Roaming in highly excited states: The central atom elimination of triatomic molecule decomposition, *Science* **383**, 746–750 (2024).
- [2] D. J. Auerbach, J. C. Tully, and A. M. Wodtke, Chemical dynamics from the gas-phase to surfaces, *Nat. Sci.* **1**, e10005 (2021).
- [3] C. D. Foley, C. Xie, H. Guo, and A. G. Suits, Orbiting resonances in formaldehyde reveal coupling of roaming, radical, and molecular channels, *Science* **374**, 1122–1127 (2021).
- [4] B. Margulis, K. P. Horn, D. M. Reich, M. Upadhyay, N. Kahn, A. Christianen, A. van der Avoird, G. C. Groenenboom, M. Meuwly, C. P. Koch, and E. Narevicius, Tomography of Feshbach resonance states, *Science* **380**, 77–81 (2023).
- [5] I. Rahinov, A. Kandratsenka, T. Schäfer, P. Shirhatti, K. Golibruch, and A. M. Wodtke, Vibrational energy transfer in collisions of molecules with metal surfaces, *Phys. Chem. Chem. Phys.* **26**, 15090–15114 (2024).
- [6] G. Meng, C. Hu, and B. Jiang, Vibrational relaxation of highly vibrationally excited molecules scattered from Au(111): Role of the dissociation barrier, *J. Phys. Chem. C* **126**, 12003–12008 (2022).
- [7] Y. Yoneda and H. Kuramochi, Rapid-scan resonant two-dimensional impulsive stimulated Raman spectroscopy of excited states, *J. Phys. Chem. A* **127**, 5276–5286 (2023).
- [8] S. O. M. Wright, I. Waldmann, and S. N. Yurchenko, Non-local thermal equilibrium spectra of atmospheric molecules for exoplanets, *Mon. Not. R. Astron. Soc.* **512**, 2911–2924 (2022).
- [9] S. O. M. Wright, S. K. Nugroho, M. Brogi, N. P. Gibson, E. J. W. de Mooij, I. Waldmann, J. Tennyson, H. Kawahara, M. Kuzuhara, T. Hirano, T. Kotani, Y. Kawashima, K. Masuda, J. L. Birkby, C. A. Watson, M. Tamura, K. Zwintz, H. Harakawa, T. Kudo, K. Hodapp, S. Jacobson, M. Konishi, T. Kurokawa, J. Nishikawa, M. Omiya,

- T. Serizawa, A. Ueda, S. Vievard, and S. N. Yurchenko, A spectroscopic thermometer: Individual vibrational band spectroscopy with the example of oh in the atmosphere of WASP-33b, *Astronomical J.* **166**, 41 (2023).
- [10] N. H. Pinkowski, Y. Ding, C. L. Strand, R. K. Hanson, R. Horvath, and M. Geiser, Dual-comb spectroscopy for high-temperature reaction kinetics, *Meas. Sci. Technol.* **31**, 055501 (2020).
- [11] A. Ehn, J. Zhu, X. Li, and J. Kiefer, Advanced laser-based techniques for gas-phase diagnostics in combustion and aerospace engineering, *Appl. Spectrosc.* **71**, 341 (2017), PMID: 28155328.
- [12] S. N. Yurchenko, W. Thiel, and P. Jensen, Theoretical ROVibrational Energies (TROVE): A robust numerical approach to the calculation of rovibrational energies for polyatomic molecules, *J. Mol. Spectrosc.* **245**, 126 (2007).
- [13] E. Mátyus, G. Czakó, and A. G. Császár, Toward black-box-type full- and reduced-dimensional variational (ro)vibrational computations, *J. Chem. Phys.* **130**, 134112 (2009).
- [14] H.-D. Meyer, F. Gatti, and G. A. Worth, eds., *Multi-dimensional Quantum Dynamics: MCTDH Theory and Applications* (Wiley, 2009).
- [15] J. M. Bowman, S. Carter, and X. Huang, MULTIMODE: A code to calculate rovibrational energies of polyatomic molecules, *Int. Rev. Phys. Chem.* **22**, 533 (2003).
- [16] O. Christiansen, A second quantization formulation of multimode dynamics, *J. Chem. Phys.* **120**, 2140–2148 (2004).
- [17] M. B. Hansen, M. Sparta, P. Seidler, D. Toffoli, and O. Christiansen, New formulation and implementation of vibrational self-consistent field theory, *J. Chem. Theory Comput.* **6**, 235–248 (2009).
- [18] O. Christiansen, Vibrational coupled cluster theory, *J. Chem. Phys.* **120**, 2149–2159 (2004).
- [19] M. J. Bramley, W. H. Green, and N. C. Handy, Vibration-rotation coordinates and kinetic energy operators for polyatomic molecules, *Mol. Phys.* **73**, 1183–1208 (1991).
- [20] E. Mátyus, A. M. S. Daría, and G. Avila, Exact quantum dynamics developments for floppy molecular systems and complexes, *Chem. Comm.* **59**, 366 (2023).
- [21] Z. Bačić and J. C. Light, Theoretical methods for rovibrational states of floppy molecules, *Annu. Rev. Phys. Chem.* **40**, 469 (1989).
- [22] J. M. Hutson, Intermolecular forces from the spectroscopy of van der waals molecules, *Annu. Rev. Phys. Chem.* **41**, 123 (1990).
- [23] I. Simkó, C. Schran, F. Briec, C. Fábri, O. Asvany, S. Schlemmer, D. Marx, and A. G. Császár, Quantum nuclear delocalization and its rovibrational fingerprints, *Angew. Chem. Int. Ed.* **62**, e202306744 (2023).
- [24] A. Yachmenev and S. N. Yurchenko, Automatic differentiation method for numerical construction of the rotational-vibrational Hamiltonian as a power series in the curvilinear internal coordinates using the Eckart frame, *J. Chem. Phys.* **143**, 014105 (2015).
- [25] X.-G. Wang and T. Carrington, Vibrational energy levels of  $\text{CH}_3^+$ , *J. Chem. Phys.* **129**, 234102 (2008).
- [26] F. Gatti, C. Iung, M. Menou, Y. Justum, A. Nauts, and X. Chapuisat, Vector parametrization of the N-atom problem in quantum mechanics. I. Jacobi vectors, *J. Chem. Phys.* **108**, 8804–8820 (1998).
- [27] C. Leforestier, A. Viel, F. Gatti, C. Muñoz, and C. Iung, The Jacobi–Wilson method: A new approach to the description of polyatomic molecules, *J. Chem. Phys.* **114**, 2099–2105 (2001).
- [28] M. J. Bramley and N. C. Handy, Efficient calculation of rovibrational eigenstates of sequentially bonded four-atom molecules, *J. Chem. Phys.* **98**, 1378–1397 (1993).
- [29] C. Iung and F. Gatti, Polyspherical parametrization of an N-atom system: Principles and applications, *Int. J. Quantum Chem.* **106**, 130–151 (2005).
- [30] F. Gatti and C. Iung, Exact and constrained kinetic energy operators for polyatomic molecules: The polyspherical approach, *Phys. Rep.* **484**, 1–69 (2009).
- [31] E. L. Klinting, D. Lauvergnat, and O. Christiansen, Vibrational coupled cluster computations in polyspherical coordinates with the exact analytical kinetic energy operator, *J. Chem. Theory Comput.* **16**, 4505–4520 (2020).
- [32] J. M. Bowman, T. Carrington, and H.-D. Meyer, Variational quantum approaches for computing vibrational energies of polyatomic molecules, *Mol. Phys.* **106**, 2145–2182 (2008).
- [33] K. Oenen, D. F. Dinu, and K. R. Liedl, Determining internal coordinate sets for optimal representation of molecular vibration, *J. Chem. Phys.* **160**, 014104 (2024).
- [34] D. Mendive-Tapia, H.-D. Meyer, and O. Vendrell, Optimal mode combination in the multiconfiguration time-dependent hartree method through multivariate statistics: Factor analysis and hierarchical clustering, *J. Chem. Theory Comput.* **19**, 1144–1156 (2023).
- [35] M. Schneider and G. Rauhut, Comparison of curvilinear coordinates within vibrational structure calculations based on automatically generated potential energy surfaces, *J. Chem. Phys.* **161**, 094102 (2024).
- [36] T. C. Thompson and D. G. Truhlar, Optimization of vibrational coordinates, with an application to the water molecule, *J. Chem. Phys.* **77**, 3031 (1982).
- [37] R. C. Mayrhofer and E. L. Sibert, Investigating optimal coordinates for describing vibrational motion, *Theor. Chim. Acta* **92**, 107–122 (1995).
- [38] J. Zúñiga, J. A. G. Picón, A. Bastida, and A. Requena, On the use of optimal internal vibrational coordinates for symmetrical bent triatomic molecules, *J. Chem. Phys.* **122**, 224319 (2005).
- [39] J. Zúñiga, A. Bastida, and A. Requena, Optimal generalized internal vibrational coordinates and potential energy surface for the ground electronic state of  $\text{SO}_2$ , *J. Chem. Phys.* **115**, 139–148 (2001).
- [40] I. W. Bulik, M. J. Frisch, and P. H. Vaccaro, Vibrational self-consistent field theory using optimized curvilinear coordinates, *J. Chem. Phys.* **147**, 044110 (2017).
- [41] J. M. Bowman, J. Zúñiga, and A. Wierzbicki, Investigations of transformed mass-scaled Jacobi coordinates for vibrations of polyatomic molecules with application to  $\text{H}_2\text{O}$ , *J. Chem. Phys.* **90**, 2708–2713 (1989).
- [42] Z. Bačić, R. B. Gerber, and M. A. Ratner, Vibrational levels and tunneling dynamics by the optimal coordinates, self-consistent field method: A study of hydrocyanic acid. *dblarw. hydroisocyanic acid*, *J. Chem. Phys.* **90**, 3606 (1986).
- [43] K. Yagi, M. Keçeli, and S. Hirata, Optimized coordinates for anharmonic vibrational structure theories, *J. Chem. Phys.* **137**, 204118 (2012).
- [44] B. Thomsen, K. Yagi, and O. Christiansen, Optimized coordinates in vibrational coupled cluster calculations, *J. Chem. Phys.* **140**, 154102 (2014).

- [45] G. Papamakarios, E. Nalisnick, D. J. Rezende, S. Mohamed, and B. Lakshminarayanan, Normalizing flows for probabilistic modeling and inference, *J. Mach. Learn. Res.* **22**, 2617 (2022).
- [46] D. Rezende and S. Mohamed, Variational inference with normalizing flows, in *Proceedings of the 32nd International Conference on Machine Learning, ICML*, Proceedings of Machine Learning Research, Vol. 37, edited by F. Bach and D. Blei (PMLR, 2015) pp. 1530–1538.
- [47] Y. Saleh and A. Iske, Inducing Riesz and orthonormal bases in  $L^2$  via composition operators, preprint (2024), arXiv:2406.18613 [math].
- [48] J. Behrmann, W. Grathwohl, R. T. Q. Chen, D. Duvenaud, and J.-H. Jacobsen, Invertible residual networks, in *Proceedings of the 36th International Conference on Machine Learning*, Proceedings of Machine Learning Research, Vol. 97, edited by K. Chaudhuri and R. Salakhutdinov (PMLR, 2019) pp. 573–582.
- [49] G. Avila and T. Carrington, Solving the Schrödinger equation using Smolyak interpolants, *J. Chem. Phys.* **139**, 134114 (2013).
- [50] W. Yang and A. C. Peet, The collocation method for bound solutions of the Schrödinger equation, *Chem. Phys. Lett.* **153**, 98 (1988).
- [51] J. Toulouse and C. J. Umrigar, Full optimization of Jastrow-Slater wave functions with application to the first-row atoms and homonuclear diatomic molecules, *J. Chem. Phys.* **128**, 174101 (2008).
- [52] A. Cuzzocrea, A. Scemama, W. J. Briels, S. Moroni, and C. Filippi, Variational principles in quantum Monte Carlo: The troubled story of variance minimization, *J. Chem. Theory Comput.* **16**, 4203 (2020).
- [53] K. L. Chubb, A. Yachmenev, J. Tennyson, and S. N. Yurchenko, Treating linear molecule HCCH in calculations of rotation-vibration spectra, *J. Chem. Phys.* **149**, 014101 (2018).
- [54] S. N. Yurchenko and T. M. Mellor, Treating linear molecules in calculations of rotation-vibration spectra, *J. Chem. Phys.* **153**, 154106 (2020).
- [55] A. A. A. Azzam, J. Tennyson, S. N. Yurchenko, and O. V. Naumenko, ExoMol molecular line lists – XVI. the rotation-vibration spectrum of hot  $\text{H}_2\text{S}$ , *Mon. Not. R. Astron. Soc.* **460**, 4063 (2016).
- [56] A. F. Al-Refaie, A. Yachmenev, J. Tennyson, and S. N. Yurchenko, ExoMol line lists – VIII. a variationally computed line list for hot formaldehyde, *Mon. Not. R. Astron. Soc.* **448**, 1704 (2015).
- [57] T. Van Mourik, G. J. Harris, O. L. Polyansky, J. Tennyson, A. G. Császár, and P. J. Knowles, Ab initio global potential, dipole, adiabatic, and relativistic correction surfaces for the hcn–hnc system, *J. Chem. Phys.* **115**, 3706 (2001).
- [58] X.-G. Wang and T. Carrington, New ideas for using contracted basis functions with a Lanczos eigensolver for computing vibrational spectra of molecules with four or more atoms, *J. Chem. Phys.* **117**, 6923 (2002).
- [59] P. M. Felker and Z. Bačić, Weakly bound molecular dimers: Intramolecular vibrational fundamentals, overtones, and tunneling splittings from full-dimensional quantum calculations using compact contracted bases of intramolecular and low-energy rigid-monomer intermolecular eigenstates, *J. Nanophotonics* **151**, 024305 (2019).
- [60] Y. Saleh, Á. F. Corral, A. Iske, J. Küpper, and A. Yachmenev, Computing excited states of molecules using normalizing flows, preprint (2023), arXiv:2308.16468 [physics].
- [61] Q. Zhang, R.-S. Wang, and L. Wang, Neural canonical transformations for vibrational spectra of molecules, *J. Chem. Phys.* **161**, 024103 (2024).
- [62] M. Entwistle, Z. Schätzle, P. A. Erdman, J. Hermann, and F. Noé, Electronic excited states in deep variational Monte Carlo, *Nat. Commun.* **14**, 274 (2023), arXiv:2203.09472 [physics].
- [63] D. Gottlieb and S. A. Orszag, *Numerical analysis of spectral methods: theory and applications* (SIAM, 1977).
- [64] K. Cranmer, S. Golkar, and D. Pappadopulo, Inferring the quantum density matrix with machine learning, arXiv preprint arXiv:1904.05903 (2019), arXiv:1904.05903 [physics].
- [65] Y. Saleh, A. Iske, A. Yachmenev, and J. Küpper, Augmenting basis sets by normalizing flows, *Proc. Appl. Math. Mech.* **23**, e202200239 (2023), arXiv:2212.01383 [math].
- [66] R. Fisher, *Statistical Methods for Research Workers*, Biological monographs and manuals (Oliver and Boyd, 1925).
- [67] T. H. Dunning, Gaussian basis sets for use in correlated molecular calculations. I. The atoms boron through neon and hydrogen, *J. Chem. Phys.* **90**, 1007 (1989).
- [68] R. A. Kendall, T. H. Dunning, Jr., and R. J. Harrison, Electron affinities of the first-row atoms revisited. Systematic basis sets and wave functions, *J. Chem. Phys.* **96**, 6796 (1992).
- [69] D. G. A. Smith, L. A. Burns, A. C. Simmonett, R. M. Parrish, M. C. Schieber, R. Galvelis, P. Kraus, H. Kruse, R. D. Remigio, A. Alenaizan, A. M. James, S. Lehtola, J. P. Misiewicz, M. Scheurer, R. A. Shaw, J. B. Schriber, Y. Xie, Z. L. Glick, D. A. Sirianni, J. S. O’Brien, J. M. Waldrop, A. Kumar, E. G. Hohenstein, B. P. Pritchard, B. R. Brooks, H. F. Schaefer, A. Y. Sokolov, K. Patkowski, A. E. DePrince, U. Bozkaya, R. A. King, F. A. Evangelista, J. M. Turney, T. D. Crawford, and C. D. Sherrill, Psi 1.4: Open-source software for high-throughput quantum chemistry, *J. Chem. Phys.* **152**, 184108 (2020).
- [70] V. Lebedev and D. Laikov, A quadrature formula for the sphere of the 131st algebraic order of accuracy, *Dokl. Math.* **59**, 477 (1999).
- [71] A. D. Becke, A multicenter numerical integration scheme for polyatomic molecules, *J. Chem. Phys.* **88**, 2547–2553 (1988).
- [72] F. M. Fernández and J. Garcia, Highly accurate potential energy curves for the hydrogen molecular ion, *Chemistry-Select* **6**, 9527–9534 (2021).

**SUPPLEMENTARY INFORMATION:  
COMPUTING EXCITED STATES OF MOLECULES USING NORMALIZING FLOWS**

Learning an optimized vibrational coordinate system  $\mathbf{r} \rightarrow g_\theta(\mathbf{r}) = \mathbf{q}$  and learning a new basis set  $\{\phi_n(\mathbf{r})\}_{n=0}^\infty \rightarrow \{\phi_n(\mathbf{q})\sqrt{|1/\det \nabla_{\mathbf{q}} g_\theta^{-1}(\mathbf{q})|}\}_{n=0}^\infty$  are two faces of the same coin, as seen, e. g., from performing a change of variable in the matrix representation of the potential

$$\mathbf{V}_{n'n} = \langle \gamma_{n'} | V | \gamma_n \rangle = \int \phi_{n'}^*(\mathbf{q}) V(g_\theta^{-1}(\mathbf{q})) \phi_n(\mathbf{q}) d\mathbf{q}.$$

In the following, we give a detailed description of the latter perspective, highlighting theoretical foundations and linking to the concept of normalizing flows in machine learning. We also provide detailed information on the numerical simulations conducted in this study, along with additional results that can facilitate the application of this method in other domains.

### MATHEMATICAL FOUNDATIONS

Composing a basis set  $\{\phi_n(\mathbf{r})\}_{n=0}^\infty$  with an invertible mapping  $g$  yields a sequence of functions  $\{\phi_n(\mathbf{q})\sqrt{|1/\det \nabla_{\mathbf{q}} g^{-1}(\mathbf{q})|}\}_{n=0}^\infty$ . Certain choices of the mapping  $g$  can produce sequences of functions with improved approximation properties [63]. A common example is the linear map  $g(x) = ax + b$ , where  $a$  and  $b$  are chosen to align the potential of the problem with the potential that generates the basis set around the equilibrium geometry of the molecule. There are also examples of nonlinear fixed mappings, such as trigonometric or exponential functions.

However, the use of adaptive nonlinear mappings introduces additional complexity. To ensure convergence of the method, the basis set must retain its completeness after compositing with the mapping  $g$ . The concept of compositing basis sets with an invertible neural network was first introduced by Cranmer *et al.* [64]. However, the approach was only applied to simple models, and the rationale for employing invertible neural networks was not fully justified or rigorously explored.

The rationale for using invertible neural networks from an approximation-theory perspective was first analyzed by Saleh *et al.* [65] and later rigorously established by Saleh and Iske [47]. They demonstrated that the augmented basis functions  $\{\phi_n(\mathbf{q})\sqrt{|1/\det \nabla_{\mathbf{q}} g^{-1}(\mathbf{q})|}\}_{n=0}^\infty$  are only complete if the nonlinear  $g$  mapping is bi-Lipschitz. For a differentiable  $g$ , this condition implies invertibility, which is necessary for the physical interpretability of the computations and means that  $g$  is a normalizing flow.

Normalizing flows are foundational models in the field of generative machine learning [45], rooted in the probability integral transform initially introduced by Fisher [66]. This theorem states that any continuous probability density  $p$

can be converted by a change of variables to a uniform distribution on the interval  $[0, 1]$ . By imposing a few reasonable conditions to  $p$ , e. g., finiteness, it can be shown that this change of variables is bijective. As a result, any pair of probability densities  $p$  and  $q$  that satisfy these reasonable conditions can be related through a change of variables, as both can be bijectively mapped into the uniform distribution.

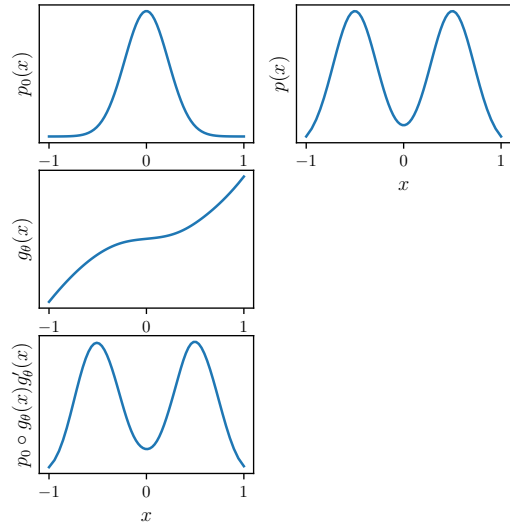


FIG. 4. An illustration of normalizing flows augmenting a single Gaussian  $p_0$ . Approximating a bi-modal distribution  $p$  with a single Gaussian is not possible. However, composing  $p_0$  with the function  $g_\theta$  produces a good approximation.

To illustrate this concept, consider the following example, which is commonly used for its simplicity. Let  $p$  an unknown bi-modal probability distribution and consider approximating the unknown distribution  $p$  by the Gaussian distribution  $p_0$ . The Gaussian distribution is a simple distribution characterized by only two parameters, the mean and the variance. However, this approximation of  $p$  via  $p_0$  is inherently flawed since no combination of the mean and the variance of  $p_0$  can make the Gaussian exhibit a bi-modal behavior. However, as discussed earlier, we can introduce an invertible change of variables  $q = g(x)$  which allows us to transform the Gaussian distribution  $p_0$  into a more complex distribution  $p^A$  that can approximate  $p$ . Specifically, we define the new distribution  $p^A$  as

$$p^A(x) = p_0(g(x)) |\det \nabla_x g(x)|,$$

where multiplying by  $|\det \nabla_x g(x)|$ , the determinant of the Jacobian of the change of variables, ensures that the distribution remains normalized. Given that both the unimodal and bimodal Gaussians are well-behaved distributions, there exists a suitable function  $g$  that can



bridge this gap. In this case, we parametrize  $g$  as an invertible function  $g_\theta$ , thus augmenting the expressivity of the simple Gaussian model. The results can be found in FIG. 4.

If the expressivity of a single Gaussian distribution can be enhanced, why not extend this approach to a family of functions, such as a basis set? This concept forms a core idea of our manuscript.

## COMPUTATIONAL DETAILS

### Construction of the Hamiltonian

The matrix elements of the kinetic energy operator in the augmented basis set are given by

$$\begin{aligned} T_{nn'} &= \int \phi_n^*(\mathbf{q}) \hat{T}(g_\theta^{-1}(\mathbf{q})) \phi_{n'}(\mathbf{q}) d\mathbf{q} \\ &= \frac{\hbar^2}{2} \sum_{kl} \int \left[ \left( \frac{1}{2\sqrt{D}} \frac{\partial D}{\partial q_k} + \sqrt{D} \frac{\partial}{\partial q_k} \right) \phi_n^*(\mathbf{q}) \right] \\ &\quad \times \sum_{\lambda\mu} \frac{\partial q_k}{\partial r_\lambda} G_{\lambda\mu}(g_\theta^{-1}(\mathbf{q})) \frac{\partial q_l}{\partial r_\mu} \\ &\quad \times \left[ \left( \frac{1}{2\sqrt{D}} \frac{\partial D}{\partial q_l} + \sqrt{D} \frac{\partial}{\partial q_l} \right) \phi_{n'}(\mathbf{q}) \right] d\mathbf{q}. \end{aligned} \quad (5)$$

Here,  $D = |1/\det \nabla_{\mathbf{q}} g_\theta^{-1}(\mathbf{q})|$ ,  $G_{\lambda\mu}$  is the kinetic-energy matrix,  $\lambda, \mu$  indices are used to denote the elements of the coordinate vector  $r$ , and  $k, l$  indices denote the elements of the coordinate vector  $q$ , i. e.,  $q_k = g_{\theta,k}(\mathbf{r})$  and  $r_\lambda = g_{\theta,\lambda}^{-1}(\mathbf{q})$ . The differential operators,  $\frac{\partial}{\partial q_k}$ , only operate inside the square brackets. To obtain this formula, we employed integration by parts, enabling the second-order derivative operator to act symmetrically on both the bra and ket functions as first-order derivatives. The boundary term is omitted as its contribution is zero for most integration domains. Additionally, the kinetic energy operator includes the so-called pseudopotential term, which originates from the transformation of coordinates from Cartesian to initial internal coordinates. It is calculated as

$$U = \frac{\hbar^2}{32} \sum_{\lambda} \sum_{\mu} \frac{G_{\lambda\mu}}{\tilde{g}^2} \frac{\partial \tilde{g}}{\partial r_\lambda} \frac{\partial \tilde{g}}{\partial r_\mu} + 4 \frac{\partial}{\partial r_\lambda} \left( \frac{G_{\lambda\mu}}{\tilde{g}} \frac{\partial \tilde{g}}{\partial r_\mu} \right), \quad (6)$$

where  $\tilde{g} = \det(G^{-1})$ . The pseudopotential is a scalar operator and its matrix elements in the transformed basis can be expressed analogously to the potential energy matrix elements in Eq. 2 of the manuscript.

A summary of the atomic masses considered in this study are provided in Table I.

TABLE I. The atomic masses utilized in calculations of the vibrational energies for the  $\text{H}_2\text{S}$ ,  $\text{H}_2\text{CO}$  and  $\text{HCN/CNH}$  molecules.

Atom	Mass (u)
Hydrogen	1.00782505
Sulfur	31.97207070
Carbon	12.0
Oxygen	15.99491463
Nitrogen	14.003074004251

### Architecture of the normalizing flow and implementation details

In this work, we employed the invertible residual neural network (iResNet) [48] to model  $g_\theta$ . An iResNet is constructed by concatenating blocks of the form

$$\mathbf{x}_{k+1} = \mathbf{x}_k + \mathbf{f}_k(\mathbf{x}_k; \theta),$$

where  $\mathbf{f}_k$  is the  $k$ -th block,  $\mathbf{x}_k$  is the input to this block, and  $\mathbf{x}_{k+1}$  is the output. We denote the initial set of coordinates as  $\mathbf{x}_0$ , and for an iResNet with  $K$  blocks, we denote its output as  $\mathbf{z} = \mathbf{x}_{K-1}$ . Each residual block is a standard feed-forward neural network composed of weights, biases and nonlinear activations. Each such block is guaranteed to be invertible if  $\mathbf{f}_k$  is Lipschitz, with Lipschitz constant  $< 1$ . The inverse of each block can be computed by a fixed-point iteration method.

To guarantee that the blocks  $\mathbf{f}_k$  for  $k = 0, \dots, K-1$  satisfy the Lipschitz condition, we used the LipSwish activation function

$$\sigma(x) := \left( \frac{1}{1.1} \right) \frac{1}{1 + \exp(-x)},$$

which has a Lipschitz constant  $\approx 1$ . A block  $\mathbf{f}_k$  containing such activation functions is thus guaranteed to be Lipschitz if each of its weight matrix  $W$  is normalized to have a spectral norm  $< 1$ . This is achieved by setting

$$W = \begin{cases} W & \text{if } \|W\|_2 < c \\ c \cdot \frac{W}{\|W\|_2} & \text{if } \|W\|_2 \geq c, \end{cases}$$

where  $0 < c < 1$  is a hyperparameter and  $\|W\|_2$  is the spectral norm of the matrix  $W$ . For a block  $\mathbf{f}_k$  containing  $n$  hidden layers, it can be shown that

$$\text{Lip}(\mathbf{f}_k) \leq c^{n+1}.$$

A special attention must be given to the architecture of each block. While a block with a Lipschitz constant close to 1 allows for a greater flexibility, a higher Lipschitz constant can significantly hinder the convergence of the fixed-point iteration method used for computing its inverse. To balance these effects, we used blocks with 2 hidden layers for all our calculations and set  $c = 0.9$ , producing blocks with Lipschitz constants  $\sim 0.7$ .

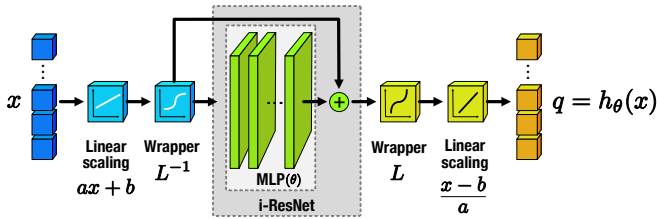


FIG. 5. Schematic diagram showing the computational workflow of the normalizing-flow function. As wrapping functions we used  $L = \tanh^{-1}(x)$ . A fixed scaling procedure was used to map the coordinates correctly to the domain of the wrapping functions. The linear scaling parameters  $a$  and  $b$  were subject to optimization together with the MLP  $\theta$ -parameters.

By construction, the iResNet imposes no restrictions to the image. However, in many computational physics and chemistry applications, the domain of internal coordinates is bounded. For example, in vibrational calculations, the internal coordinates often represent distances which are strictly positive, or angles, which are typically confined to a finite interval, such as  $\pi$  or  $2\pi$ . Mapping into non-physical or redundant ranges of internal coordinates can lead to inaccurate numerical results and breaking of the variational limit. For example, the iResNet output may fall within coordinate regions where the potential is undefined.

To address these issues, we developed an invertible workflow that enables control over the output ranges. First, we mapped the ranges of the quadratures of the basis sets in each dimension to  $[-1, 1]$  using a fixed linear scaling. We then applied a wrapping function  $L$  that maps this interval to an infinite interval, allowing the

iResNet to operate in this unbounded domain where its image is equivalent to its domain. Next, we mapped the output of the iResNet back to the  $[-1, 1]$  interval by applying the inverse of the wrapper  $L^{-1}$ . Finally, we used a linear scaling  $\mathbf{a} \cdot \mathbf{x} + \mathbf{b}$  to map the output to the desired target interval, with this scaling optimized. To ensure the output remains within the correct interval, we used a subparametrization of the linear parameters  $a_i(\alpha), b_i(\beta)$ , where  $\alpha$  and  $\beta$  are optimized. For different coordinates we applied different functions for infinite, semi-infinite and finite intervals, depending on the coordinate specific range requirements.

A schematic of this workflow is provided in Figure FIG. 5.

### Comparison against reference data

Benchmark results for vibrational energy calculations were generated using the wavefunction ansatz described in Eq. 3 of the manuscript. The calculations employed a basis polyad truncation  $P_{\max} = 36$  for  $\text{H}_2\text{S}$ ,  $P_{\max} = 13$  for  $\text{H}_2\text{CO}$ , and  $P_{\max} = 44$  and for  $\text{HCN}/\text{HCN}$ . We compared our results with those of Azzam *et al.* [55] for  $\text{H}_2\text{S}$ , Al-Refaie *et al.* [56] for  $\text{H}_2\text{CO}$ , and Van Mourik *et al.* [57] for  $\text{HCN}/\text{HNC}$ .

In Table II, we present the deviations  $\Delta E_i = E_i - E_i^{\text{ref}}$  between our calculated energies  $E_i$  and the reference values,  $E_i^{\text{ref}}$  across one  $i = 1..100$  lowest energy levels for the three molecular systems. The results demonstrate almost exact agreement with the reference data, with most of the states converging to even lower limits than the reference data.

TABLE II: Comparison of vibrational energies (in  $\text{cm}^{-1}$ ) of  $\text{H}_2\text{S}$ ,  $\text{HCN}/\text{CNH}$ , and  $\text{H}_2\text{CO}$  molecules, calculated using the normalizing-flow approach  $E_i$ , with reference energies  $E_i^{\text{ref}}$  [55–57], across the 100 lowest vibrational states. Deviations  $\Delta E_i$  are defined as the absolute differences between calculated  $E_i$  and reference  $E_i^{\text{ref}}$  energies.

$i$	$\text{H}_2\text{S}$			$\text{HCN}$			$\text{H}_2\text{CO}$		
	$E_i$	$E_i^{\text{ref}}$	$\Delta E_i$	$E_i$	$E_i^{\text{ref}}$	$\Delta E_i$	$E_i$	$E_i^{\text{ref}}$	$\Delta E_i$
1	0.00	0.00	0.00	0.00	0.00	0.00	0.00	0.00	0.00
2	1182.57	1182.58	0.01	1414.92	1414.92	0.00	1167.35	1167.34	0.01
3	2353.91	2353.96	0.06	2100.58	2100.58	0.00	1249.25	1249.07	0.18
4	2614.39	2614.41	0.01	2801.46	2801.46	0.00	1500.16	1500.12	0.04
5	2628.46	2628.45	0.01	3307.74	3307.75	0.01	1745.72	1746.05	0.33
6	3513.70	3513.79	0.09	3510.99	3510.99	0.00	2327.42	2327.50	0.08
7	3779.19	3779.17	0.02	4176.24	4176.24	0.00	2422.65	2422.63	0.02
8	3789.27	3789.27	0.00	4181.46	4181.45	0.01	2494.41	2494.32	0.09
9	4661.61	4661.67	0.07	4686.28	4686.29	0.01	2666.89	2667.04	0.14
10	4932.69	4932.70	0.01	4891.76	4891.76	0.00	2719.13	2719.08	0.05
11	4939.13	4939.10	0.03	5185.57	5185.64	0.07	2782.23	2782.41	0.18
12	5145.03	5144.99	0.05	5394.43	5394.43	0.00	2843.35	2843.34	0.01
13	5147.17	5147.22	0.05	5537.76	5537.76	0.00	2905.84	2905.86	0.03
14	5243.16	5243.10	0.06	5586.50	5586.50	0.00	2999.02	2999.01	0.01
15	5797.21	5797.23	0.03	6033.72	6033.72	0.00	3000.63	3000.00	0.62
16	6074.57	6074.58	0.02	6127.51	6127.56	0.05	3238.71	3238.94	0.23
17	6077.63	6077.59	0.03	6242.43	6242.42	0.00	3470.13	3471.72	1.59
18	6288.13	6288.15	0.01	6260.59	6260.59	0.00	3481.16	3481.30	0.14
19	6289.13	6289.17	0.04	6513.48	6513.50	0.02	3585.81	3585.89	0.08
20	6385.32	6385.32	0.00	6768.51	6768.51	0.00	3675.21	3675.21	0.00

21	6920.08	6920.08	0.00	6879.60	6879.60	0.00	3737.68	3737.05	0.63
22	7204.31	7204.31	0.00	6960.99	6960.99	0.00	3825.52	3825.97	0.45
23	7204.43	7204.44	0.00	7088.71	7088.74	0.03	3887.23	3887.36	0.13
24	7419.85	7419.85	0.00	7210.51	7210.59	0.08	3936.92	3936.44	0.49
25	7420.08	7420.09	0.02	7369.18	7369.18	0.00	3941.41	3941.53	0.12
26	7516.83	7516.83	0.00	7461.59	7461.60	0.01	3996.37	3996.48	0.11
27	7576.41	7576.38	0.03	7617.24	7617.24	0.00	4023.10	4022.56	0.54
28	7576.60	7576.54	0.05	7641.28	7641.28	0.00	4057.79	4058.10	0.31
29	7752.34	7752.26	0.08	7855.83	7855.84	0.01	4083.99	4083.49	0.50
30	7779.35	7779.32	0.03	8020.41	8020.45	0.04	4164.11	4164.13	0.02
31	8029.82	8029.81	0.00	8110.25	8110.25	0.00	4164.74	4165.27	0.53
32	8318.68	8318.68	0.00	8140.64	8140.69	0.05	4193.47	4193.19	0.28
33	8321.86	8321.86	0.00	8197.55	8197.55	0.00	4247.88	4247.61	0.27
34	8539.57	8539.56	0.00	8283.37	8283.37	0.00	4256.27	4256.31	0.04
35	8539.82	8539.82	0.00	8323.52	8323.52	0.00	4335.29	4335.11	0.17
36	8637.16	8637.16	0.00	8584.71	8584.74	0.03	4397.82	4398.13	0.31
37	8697.13	8697.14	0.01	8691.66	8691.67	0.01	4467.75	4467.12	0.63
38	8697.18	8697.16	0.02	8830.27	8830.27	0.00	4495.51	4495.50	0.01
39	8878.59	8878.59	0.00	8850.65	8850.74	0.09	4530.64	4529.64	1.01
40	8897.38	8897.38	0.00	8945.48	8945.50	0.02	4572.74	4571.66	1.08
41	9126.10	9126.09	0.01	8954.46	8954.47	0.01	4624.01	4623.93	0.08
42	9420.24	9420.24	0.00	9009.00	9009.00	0.00	4629.12	4629.22	0.10
43	9426.39	9426.39	0.00	9088.01	9088.05	0.04	4730.71	4730.04	0.66
44	9647.10	9647.17	0.07	9164.06	9164.08	0.02	4737.47	4734.33	3.14
45	9647.61	9647.61	0.00	9214.77	9214.85	0.08	4741.35	4741.40	0.06
46	9745.80	9745.80	0.00	9440.11	9440.12	0.01	4840.74	4840.80	0.06
47	9806.71	9806.67	0.05	9488.55	9488.54	0.01	4926.85	4926.53	0.32
48	9806.75	9806.73	0.01	9508.91	9508.91	0.00	4953.11	4956.91	3.80
49	9911.10	9911.02	0.08	9619.20	9619.29	0.09	4977.69	4978.25	0.55
50	9911.11	9911.02	0.09	9674.67	9674.67	0.00	4980.56	4978.44	2.12
51	9993.68	9993.68	0.00	9675.25	9675.25	0.00	5041.90	5042.22	0.32
52	10004.98	10004.98	0.00	9743.71	9743.79	0.08	5092.09	5092.58	0.48
53	10188.36	10188.36	0.00	9865.30	9865.33	0.03	5109.53	5109.39	0.15
54	10194.51	10194.45	0.06	9922.90	9922.92	0.02	5140.99	5141.01	0.02
55	10208.85	10208.77	0.08	9993.94	9993.95	0.01	5155.95	5154.39	1.55
56	10292.54	10292.54	0.00	10006.55	10006.59	0.04	5173.88	5177.65	3.78
57	10508.45	10508.45	0.00	10132.33	10132.38	0.05	5187.10	5187.25	0.14
58	10517.60	10517.59	0.01	10165.62	10165.60	0.02	5204.71	5205.00	0.30
59	10742.14	10742.14	0.00	10266.38	10266.40	0.02	5246.47	5246.39	0.07
60	10742.73	10742.73	0.00	10304.11	10304.10	0.01	5256.28	5256.28	0.00
61	10842.18	10842.18	0.00	10364.93	10364.90	0.03	5313.40	5312.86	0.54
62	10904.69	10904.69	0.00	10460.51	10460.50	0.01	5321.29	5322.42	1.13
63	10904.77	10904.77	0.00	10636.68	10636.70	0.02	5325.56	5325.30	0.26
64	11008.77	11008.70	0.08	10654.81	10654.87	0.06	5357.78	5358.09	0.31
65	11008.79	11008.77	0.01	10749.73	10749.70	0.03	5387.97	5386.43	1.54
66	11097.17	11097.17	0.00	10753.95	10753.98	0.03	5415.35	5415.83	0.48
67	11101.53	11101.53	0.00	10758.04	10758.00	0.04	5417.78	5417.91	0.13
68	11278.43	11278.08	0.35	10861.98	10862.15	0.17	5432.36	5433.31	0.95
69	11291.96	11291.96	0.00	10871.09	10871.10	0.01	5461.66	5463.15	1.49
70	11294.93	11294.93	0.00	10922.00	10922.03	0.03	5489.64	5490.04	0.40
71	11391.68	11391.68	0.00	10925.18	10925.30	0.12	5491.88	5490.58	1.30
72	11582.90	11582.88	0.02	11006.52	11006.50	0.02	5531.54	5532.38	0.84
73	11595.17	11595.14	0.04	11035.70	11035.70	0.00	5544.66	5544.61	0.04
74	11824.14	11824.13	0.00	11065.18	11065.23	0.05	5552.75	5552.88	0.13
75	11824.66	11824.65	0.00	11198.41	11198.51	0.10	5626.23	5626.49	0.26
76	11925.75	11925.75	0.00	11225.82	11225.90	0.08	5651.44	5651.16	0.28
77	11990.55	11990.55	0.00	11271.68	11271.70	0.02	5659.78	5660.99	1.21
78	11990.65	11990.65	0.00	11489.39	11489.40	0.01	5668.63	5667.46	1.17
79	12095.40	12095.40	0.00	11536.09	11536.10	0.01	5681.36	5681.46	0.10
80	12095.44	12095.44	0.00	11539.63	11539.71	0.08	5689.12	5688.23	0.88
81	12149.52	12149.46	0.06	11549.66	11549.60	0.06	5718.96	5718.83	0.13
82	12149.55	12149.52	0.04	11589.99	11590.02	0.03	5731.83	5732.19	0.37
83	12186.40	12186.40	0.00	11672.67	11672.80	0.13	5766.91	5766.91	0.01

84	12188.55	12188.55	0.00	11688.05	11688.10	0.05	5768.19	5769.06	0.87
85	12336.05	12334.64	1.41	11710.13	11710.10	0.03	5773.57	5771.67	1.89
86	12383.69	12383.69	0.00	11744.32	11744.36	0.04	5810.02	5809.85	0.18
87	12384.60	12384.60	0.00	11744.36	11744.50	0.14	5823.14	5822.71	0.43
88	12481.05	12481.05	0.00	11832.45	11832.49	0.04	5887.76	5888.44	0.69
89	12524.83	12524.64	0.20	11969.83	11969.90	0.07	5889.05	5888.55	0.50
90	12525.35	12525.21	0.13	11970.23	11970.27	0.04	5890.67	5890.16	0.52
91	12643.38	12643.27	0.10	11977.84	11977.70	0.14	5937.71	5937.06	0.65
92	12659.10	12658.92	0.17	12055.72	12055.70	0.02	5985.56	5985.33	0.23
93	12695.20	12695.20	0.00	12102.62	12102.69	0.07	5988.14	5988.05	0.10
94	12735.21	12735.21	0.00	12192.45	12192.50	0.05	5997.65	5997.93	0.29
95	12892.54	12892.52	0.01	12200.53	12200.60	0.07	5999.87	5999.46	0.41
96	12892.84	12892.83	0.01	12304.49	12304.50	0.01	6054.73	6053.56	1.17
97	12995.97	12995.95	0.01	12311.73	12311.70	0.03	6094.22	6093.56	0.66
98	13063.69	13063.69	0.00	12374.87	12375.11	0.24	6107.86	6108.32	0.45
99	13063.80	13063.80	0.00	12382.04	12382.00	0.04	6124.37	6124.52	0.15
100	13170.37	13170.37	0.00	12384.74	12384.75	0.01	6179.72	6178.84	0.8

## FURTHER INVESTIGATIONS

### Convergence with respect to enhancement of normalizing-flow complexity

In spectral methods, the standard approach for improving the accuracy of computed energy levels is to increase the number of basis functions  $N$ . However, this can be computationally expensive, with memory costs scaling as  $N^2$  and certain computational tasks, such as diagonalization of the Hamiltonian matrix, scaling up to  $N^3$ . The normalizing-flow approach offers a possibility of enhancing the expressivity of the basis functions by creating a more complex mapping, achieved by adding additional blocks. In FIG. 6, we show the sum of the 100 lowest vibrational energies (loss) of the HCN/CNH isomers as a function of the number of blocks in the iResNet model, for a fixed number of basis functions (at  $P_{\max} = 16$ ).

### Transferability of the normalizing flow across different basis set truncation levels

During our investigations into the interpretability of the normalizing-flow coordinates, we noticed that the optimized coordinates remain consistent across different basis set truncation levels  $P_{\max}$ . This observation prompted us to explore the transferability of the normalizing flow across different truncation levels. Interestingly, we found that a normalizing flow trained with few basis functions could effectively transfer to larger basis sets without the need for retraining. In FIG. 7, we demonstrate this by comparing the vibrational energy levels of HCN/CNH using a normalizing flow initially trained to minimize the sum of the lowest 200 energies with a basis truncated at  $P_{\max} = 32$ . This mapping was then used with basis sets truncated at  $P_{\max} > 32$  and compared to the results of calculations where the normalizing flow was optimized for each truncation level.

The results in FIG. 7 reveal that the transferred normalizing-flow mapping provides comparable accuracy to the optimized mapping for each truncation level and performs significantly better than Jacobi coordinates.

It is worth highlighting that transferability enables significant computational savings. Expanding calculations to incorporate a larger number of basis functions is feasible as long as the quantities dependent on normalizing flow, such as  $\frac{\partial q_\alpha}{\partial r_i}$ ,  $\frac{\partial D}{\partial r_i}$ ,  $\frac{1}{D}$ , etc, can be efficiently stored in memory or recomputed on the fly. Importantly, the size and computation cost of these quantities are independent of the basis size, meaning that calculations using a pre-trained normalizing flow scale with basis size in the same way as those using a regular linear mapping.

Based on these observations, we propose the following efficient protocol for implementing our approach: (i) Train a normalizing flow on a small basis set and store the optimized parameters. (ii) Transfer the learned coordinates to a larger basis set where training would be computationally prohibitive, then solve the eigenvalue problem using the pre-trained normalizing flow to obtain accurate energy levels. This protocol is particularly useful for high dimensional systems, where training costs are significantly higher.

### Electronic calculations

The nonlinear ansatz described in Eq. 3 of the manuscript can be used to solve the electronic Schrödinger equation. To demonstrate this, we computed electronic states of prototypical one-electron systems such as the hydrogen atom,  $\text{H}_2^+$  molecular ion, and carbon atom in the single-active electron approximation. We only consider normalizing flows for the radial coordinate and integrated out the angular coordinates using the spherical-harmonic basis. This approach is consistent with common practices in quantum chemistry, where the radial basis typically presents the primary challenge and is the main target of

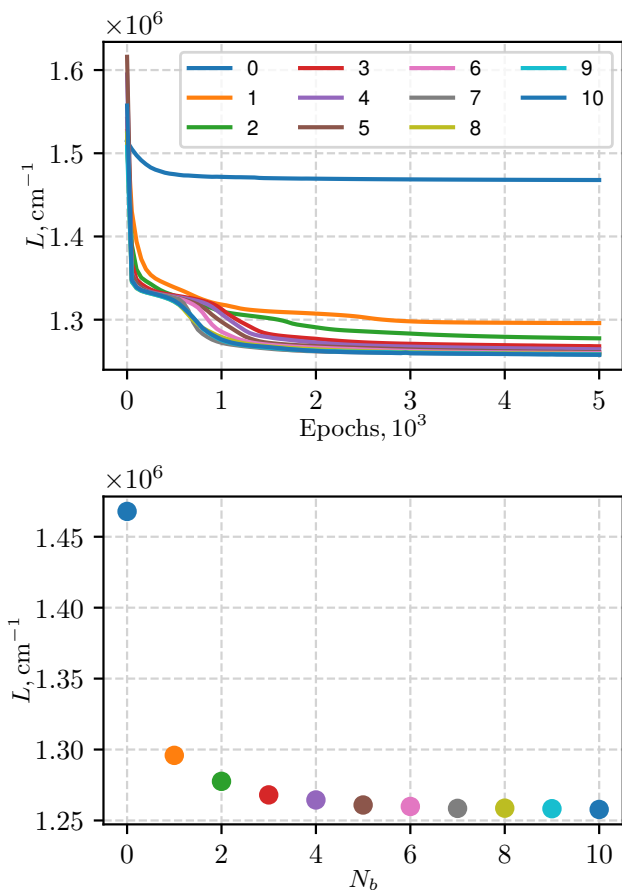


FIG. 6. Convergence of the sum of the lowest 100 vibrational energy levels  $L = \sum_i^{100} E_i$  for HCN/CNH as a function of the number of blocks in the iResNet model  $N_b$ . The upper plot shows the convergence of this sum over the number of optimization epochs, with results for different  $N_b$  represented by different colors. The lower plot shows the convergence of the optimized sum as a function of  $N_b$ .

optimization. As a starting basis we explored Hermite basis, the basis of three-dimensional isotropic harmonic oscillator, and the standard atomic-orbital basis sets from Dunning’s family [67, 68]. The number of basis functions was defined by the number of radial functions.

The Hamiltonians for the one-electron radial problems were derived by integrating out the angular coordinates using spherical-harmonic functions  $Y_{l,m}$  as the angular basis, or solid-harmonic functions  $r^l Y_{l,m}$  in the case of atomic-orbital basis sets. For the Hermite and isotropic harmonic oscillator radial basis sets, we utilized a direct product of the radial and angular basis functions with  $l \leq l_{\max}$ , where  $l_{\max} = 3$  for atoms and 8 for molecules. For the atomic-orbital basis set, we employed specific combinations of radial Gaussian and solid-harmonic functions as dictated by the structure of the basis sets.

The angular matrix elements of the electron-nuclei Coulomb-attraction potential were computed using the

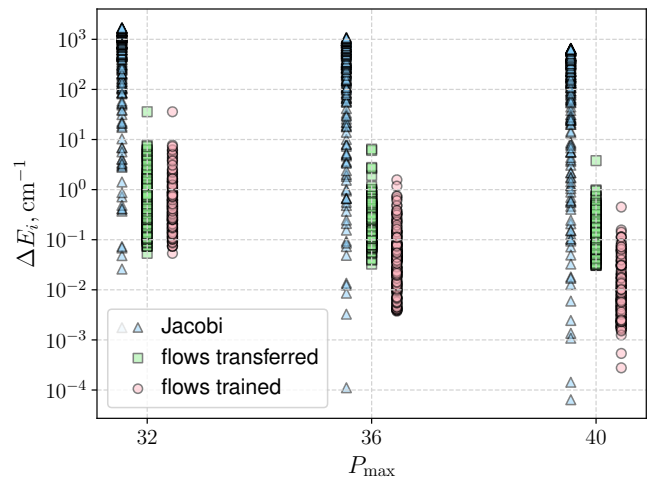


FIG. 7. Convergence of the lowest 200 vibrational energy levels ( $E_i, i = 1..200$ ) for HCN/CNH, calculated using Jacobi coordinates (triangles, light blue), normalizing-flow coordinates transferred from  $P_{\max} = 32$  (squares, light green), and optimized normalizing-flow coordinates (circles, light pink). The energy discrepancies ( $\Delta E_i$ ) relative to our converged benchmark reference are shown for basis sets truncated at  $P_{\max} = 32$  (1785 basis functions), 36 (2470), and 40 (3311). All states are slightly offset along the  $P_{\max}$  axis for visual clarity.

Laplace expansion, with truncation determined by  $l_{\max}$  of the angular basis.

The electronic energies of multi-electron systems, e.g., carbon atom, were calculated using the single-active-electron approximation, in which the electron-electron Coulomb-interaction potential is approximated by the one-electron electrostatic potential created by the electron density  $\rho(\mathbf{r})$  of a singly-charged ion in the ground state, i.e.,

$$V(\mathbf{r}) = - \int \frac{\rho(\mathbf{r}')}{|\mathbf{r} - \mathbf{r}'|} d\mathbf{r}'.$$

In addition, the exchange-interaction potential is generally added using some popular approximations, like the local-density approximation models. Our focus is primarily on investigating the basis set convergence of energies and its enhancement *via* normalizing flows. The absolute accuracy of the electronic energies was not our primary concern, hence we did not include the exchange-interaction potential in our calculations.

In simulations for carbon atom, the one-electron electrostatic potential of  $\text{C}^+$  was calculated using the second-order approximate coupled-cluster CC2 level of theory with the aug-cc-pV5Z atomic-orbital basis set [67, 68], as implemented in the Psi4 quantum chemistry package [69]. The calculations were performed on a grid generated by the direct product of an equidistant radial grid  $\{r_g\}_g^{N_g}$  and the Lebedev quadrature grid of 131st order represented by a set of angular points  $\{\theta_h, \phi_h\}_h^{N_h}$  [70]. The radial potential was calculated by integrating angular coordinates

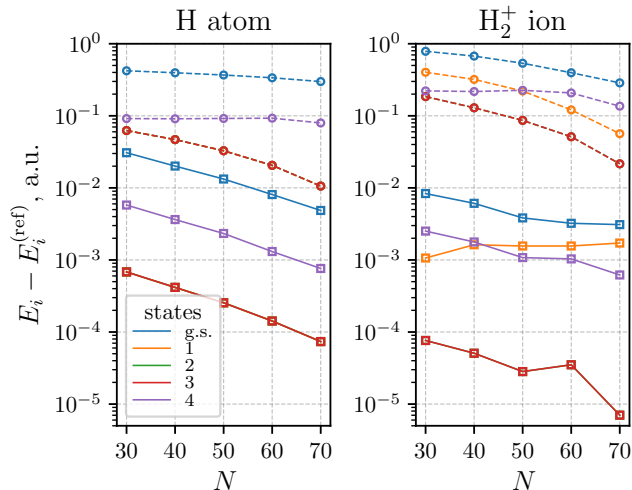


FIG. 8. Convergence of the ground (g.s.) and four lowest excited electronic states of hydrogen atom and hydrogen molecular ion  $\text{H}_2^+$  ( $R_{\text{H-H}} = 2$  Bohr) plotted against the number of Hermite radial basis functions  $N$ . Results obtained with optimized-linear (dashed, circles) and normalizing-flow (solid, squares) parameterizations are compared. The reference energies  $E_i^{\text{ref}}$  for  $\text{H}_2^+$  are from Fernández and Garcia [72].

at each radial point in the basis of spherical-harmonic functions using Lebedev quadrature rule, i. e.,

$$V_{l'm',lm}(r_g) = \langle Y_{l'm'}(\theta, \phi) | V(r_g, \theta, \phi) | Y_{lm}(\theta, \phi) \rangle \\ \approx \sum_h^{N_h} w_h Y_{l'm'}^*(\theta_h, \phi_h) Y_{lm}(\theta_h, \phi_h) V(r_g, \theta_h, \phi_h),$$

where  $w_h$  is the Lebedev quadrature weight including spherical volume element. For computing the angular integrals between the spherical harmonics centered at different centers, which are needed in atomic-orbital-basis calculations for molecules, we also implemented Becke’s partitioning scheme [71]. The calculated values of the radial potential  $V_{l'm',lm}(r_g)$  were interpolated across the radial grid  $\{r_g\}_g^{N_g}$  using the regular grid interpolator technique.

The reference energies for the hydrogen atom are known analytically, while for the hydrogen-molecule cation  $\text{H}_2^+$ , the energies calculated using the Riccati-Padé method [72] were employed as the reference. In Table III, we present the absolute errors for the ground and four lowest excited electronic states of H atom and  $\text{H}_2^+$ , as calculated using normalizing flows with different basis sets. For comparison, the table also includes errors corresponding to full-configuration interaction calculations in large atomic-orbital basis sets aug-cc-pV5Z and aug-cc-pV6Z [67, 68], as computed using the Psi4 quantum chemistry package [69].

The application of the normalizing-flow ansatz with Hermite basis set demonstrates high accuracy and fast

H atom			
State	Hermite	iso-HO	AV6Z
Ground	-4.8	-0.02	-0.0007
1st excited	-0.07	-0.002	-0.08
2d excited	-0.07	-0.002	-1.22
3d excited	-0.07	-0.002	-1.22
4th excited	-0.8	-0.002	-1.22
$\text{H}_2^+$ ion			
State	Hermite	AV5Z	
Ground	-3.1	-0.01	
1st excited	-1.7	-0.01	
2d excited	-0.007	-0.44	
3d excited	-0.007	-0.44	
4th excited	-0.62	-0.53	

TABLE III. The errors (exact – calculated, in mHartree) in the ground and excited state calculations for H atom and  $\text{H}_2^+$  ( $R_{\text{H-H}} = 2$  Bohr), using normalizing flows with Hermite and three-dimensional isotropic harmonic oscillator (iso-HO) basis sets. For comparison, errors corresponding to full-configuration interaction approach with aug-cc-pV6Z (AV6Z) basis for H and aug-cc-pV5Z (AV5Z) basis for  $\text{H}_2^+$  are also listed. Note that the normalizing-flow calculations of  $\text{H}_2^+$  employed s single-center spherical-harmonic basis truncated at  $l_{\text{max}} = 8$ , which accounts for estimated  $-1.1, -0.2, -10^{-5}, -10^{-5}, -0.15$  mHartree differences in the corresponding electronic energies.

basis-set convergence for the radial electronic problem, although such basis is typically considered unsuitable for solving electronic problems. In FIG. 8, we show the convergence of the electronic energies for H atom and  $\text{H}_2^+$  molecular ion as a function of the number of Hermite radial basis functions  $N$ . The results are compared against the linear parametrization, obtained by setting  $g(\mathbf{x}) = \mathbf{a} \cdot \mathbf{x} + \mathbf{b}$  in Eq. 3 of the manuscript, where the linear parameters  $\mathbf{a}$  and  $\mathbf{b}$  were optimized. Using the normalizing-flow ansatz, the electronic energies of H and  $\text{H}_2^+$  converge very quickly to within few mHartree of the exact values for the ground state, respectively, and even more precisely for the excited states. The accuracy for  $\text{H}_2^+$  is constrained to  $\sim 1$  mHartree for the ground state and less than that for excited states due to truncation in the angular basis set. When employing a linear parametrization, a considerably larger number of Hermite-basis functions would be required to reach the same accuracy.

Normalizing flows also improved the performance of more common basis sets used in electronic structure computations, such as the basis set of isotropic three-dimensional harmonic oscillator (iso-HO) and the augmented correlation-consistent aug-cc-pVXZ ( $X=\text{D, T, Q, 5, 6}$ ) atomic orbital basis sets from Dunning’s family [67, 68]. Results for hydrogen atom are presented in FIG. 9, illustrating that the iso-HO basis set, while inherently well-suited and fast-converging for the problem, still exhibits a notable enhancement in accuracy when

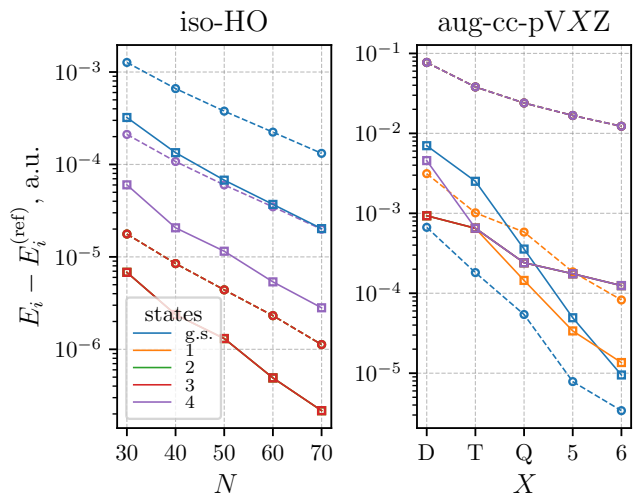


FIG. 9. Convergence of the ground (g.s.) and four lowest excited electronic states of hydrogen atom plotted against the size of the radial basis, for the three-dimensional isotropic harmonic oscillator (iso-HO) and atomic-orbital (aug-cc-pVXZ) basis sets. Results obtained with fixed-linear (circles, dashes) and normalizing-flow (solid, squares) parameterizations are compared. Since the four excited states of the hydrogen atom are degenerate, this results in indistinguishable and overlapping error values in some of the plots.

composed with a normalizing flow. Although the original atomic-orbital basis set demonstrates quicker ground-state convergence compared to that composed with a normalizing flow, the latter yields results that are more accurate and fast-converging for excited states. The lack of improvement in the ground-state energy by normalizing flow is likely due to the nature of atomic orbital basis sets, which consist of Gaussian functions with exponents carefully optimized for the ground state of an atom. This specific optimization likely accounts for ineffectiveness of normalizing flow in improving the ground electronic energy.

In FIG. 10, we show the convergence for the ground and four lowest excited electronic states of carbon atom with the number of radial basis functions, as calculated using the normalizing-flow approach and an optimized-linear parametrization. The convergence is plotted for different basis sets, including the Hermite basis set, the isotropic three-dimensional harmonic oscillator basis sets, and augmented correlation-consistent atomic orbital basis sets. The data clearly shows that the normalizing-flow approach generally improves the accuracy of results for all states across different basis sets, compared to optimized-linear mapping. However, an exception can be noted in the case of atomic-orbital basis sets. While normalizing-flow parametrization leads to faster convergence for the

ground and first excited states, it exhibits comparative or slightly inferior accuracy for the remaining excited states, particularly with smaller basis sets, as compared

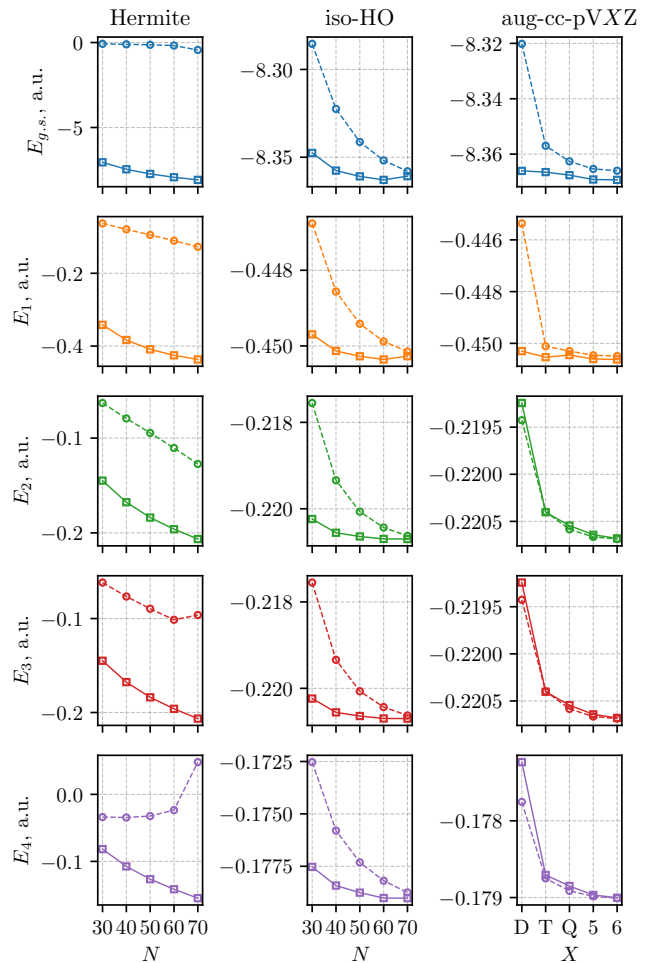


FIG. 10. Convergence of the ground (g.s.) and four lowest excited electronic energies of carbon atom plotted against the size of the radial basis  $N$  (or  $X$ ), for the Hermite, three-dimensional isotropic harmonic oscillator (iso-HO) and atomic-orbital (aug-cc-pVXZ) basis sets. Results obtained with optimized-linear (circles, dashed lines) and normalizing-flow (squares, solid lines) parameterizations are compared. The energies are calculated using the single-active-electron approximation with the Coulomb potential obtained from a quantum chemical calculation and neglecting the exchange-interaction potential.

to an optimized-linear mapping. We also noticed some convergence issues of the training procedure with a larger number of basis functions, which can be attributed to the limitations in the accuracy of numerical integration with Hermite and Laguerre quadratures used for calculations across all basis sets.